

MAY 10 2024

Inference of source signatures of merchant ships in shallow ocean environments^{a)}

D. P. Knobles; Tracianne B. Neilsen; William S. Hodgkiss; John A. Goff



J. Acoust. Soc. Am. 155, 3144–3155 (2024)

<https://doi.org/10.1121/10.0025983>



ASA

Advance your science and career as a member of the
Acoustical Society of America

[LEARN MORE](#)

Inference of source signatures of merchant ships in shallow ocean environments^{a)}

D. P. Knobles,^{1,b)} Tracianne B. Neilsen,² William S. Hodgkiss,^{3,c)} and John A. Goff⁴

¹Knobles Scientific and Analysis, LLC, Austin, Texas 78731, USA

²Department of Physics and Astronomy, Brigham Young University, Provo, Utah 84602, USA

³Scripps Institute of Oceanography, University of California at San Diego, La Jolla, California 92037, USA

⁴Institute for Geophysics, University of Texas at Austin, Austin, Texas 78758, USA

ABSTRACT:

An ocean acoustics experiment in 2017 near a shipping lane on the New England continental shelf in about 75 m of water provided an opportunity to evaluate a methodology to extract source signatures of merchant ships in a bottom-limited environment. The data of interest are the received acoustic levels during approximately 20 min time intervals centered at the closest position of approach (CPA) time for each channel on two 16-element vertical line arrays. At the CPA ranges, the received levels exhibit a frequency-dependent peak and null structure, which possesses information about the geophysical properties of the seabed, such as the porosity and sediment thickness, and the characterization of the source, such as an effective source depth. The modeled seabed is represented by two sediment layers, parameterized with the viscous grain shearing (VGS) model, which satisfies causality, over a fixed deep layered structure. Inferred estimates of the implicit source levels require averaging an error function over the full 20 min time intervals. Within the 200–700 Hz band, the Wales–Heitmeyer model captures the inferred frequency dependence of the source levels. © 2024 Acoustical Society of America. <https://doi.org/10.1121/10.0025983>

(Received 15 December 2023; revised 20 April 2024; accepted 25 April 2024; published online 10 May 2024)

[Editor: Christ de Jong]

Pages: 3144–3155

I. INTRODUCTION

The modeling and measurement of the frequency-dependent source level, $SL(f)$, of merchant ships (Gray and Greeley, 1980; McKenna *et al.*, 2012; Gassmann *et al.*, 2017) continue to be of importance because merchant shipping represents the largest source of anthropogenic noise in the ocean. While the inference of $SL(f)$ in deep ocean environments is relatively straightforward, to accomplish this in shallow water remains one of the most challenging problems in ocean acoustics (Crocker *et al.*, 2014; Jiang *et al.*, 2020; Tollefsen *et al.*, 2022; MacGillivray *et al.*, 2023). The ability to characterize the sound propagation in bottom-limited regions is generally more complicated in part because the frequency-dependent propagation loss [PL(f)] becomes more sensitive to the geoacoustic properties of seabed. This in turn complicates the inference of $SL(f)$, which requires knowledge of the PL(f). First, noise, model errors, and parameter ambiguities of a geoacoustic model limit the range accuracy of modeled PL(f). Second, because of the random temporal variability and aspect dependence of $SL(f)$, any inference methodology needs to average $SL(f)$ over some minimal time/range interval of observation. No simple approach exists to find an optimal solution to what we refer to as the shallow-water *range dilemma*.

The proposed solution to the range dilemma is a two-step process that utilizes a prior geophysical model, which assumes a two-layered seabed sediment parametrization of the viscous grain shearing (VGS) model (Buckingham, 2000, 2007) over a fixed deep seabed sediment. First, for each random sampling of the source depth, the closest position of approach (CPA) range, and the VGS hypothesis space θ , the SL_j , $SL(\theta, f, z_j)$, for $(j = 1, 2, \dots, N_r - 1, N_r)$, is estimated implicitly (Dosso and Wilmut, 2006; Knobles, 2015), where z_j is the receiver depth of the j th hydrophone of the vertical line array (VLA), and N_r is the number of receivers. This SL_j is an average over the full time interval of a time-symmetric spectrogram. Second, the inversion method exploits the broadband coherent structure of the acoustic intensity at the CPA time. The main idea is the acoustic field at CPA over a large enough frequency band may possess sufficient information content about the properties of the source-receiver geometry and the acoustical properties of the seabed to permit a statistical inference of $SL(f, z_j)$. This concept may be viewed as a variant of a recently reported idea called feature-based inversion (Knobles *et al.*, 2021; Knobles *et al.*, 2022). The estimated time-averaged $SL(\theta, z_j, f_k)$ is used to evaluate the error function at the CPA range (corresponding to $t_i = t_{cpa}$). The statistics of the CPA-based error function are then utilized to estimate sediment parameters of the VGS model, the source depth, the CPA range, and the SL_j .

As a test of the efficacy of the proposed methodology, this study takes advantage of the placement of VLAs near a

^{a)}This paper is part of a special issue on Verification and Validation of Source and Propagation Models for Underwater Sound.

^{b)}Email: dpknobles@kphysics.org

^{c)}Email: whodgkiss@ucsd.edu

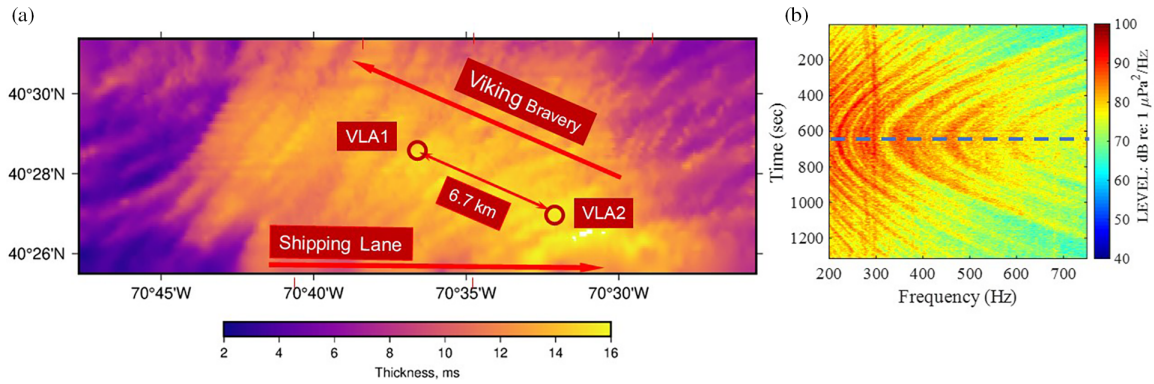


FIG. 1. (Color online) (a) Schematic of the experimental measurement area on top of a two-way travel-time of mud-layer map and (b) an example of a measured spectrogram on VLA 02 channel 05 from the ship *Kalamata*. The dotted blue line designates CPA time.

shipping lane in the New England Mudpatch during the Seabed Characterization Experiment (SBCEXP) in 2017 (Wilson *et al.*, 2020). The measurements were made during benign water column conditions. Data samples were processed in the 200–750 Hz band, where the sound radiation of the ships is mostly characterized by continuous broadband noise generated by cavitation at the rotating propeller. Estimates of seabed and source parameters are obtained from optimal solutions of the parameter space and the properties of parameter marginal probability density functions (PDFs) derived from a maximum entropy approach. The $PL(f)$ values for these solutions in the parameter space are used to estimate $SL(\hat{\theta}, f)$, where $\hat{\theta}$ is the parameter vector that minimizes an error function. The estimated $SL(\hat{\theta}, f)$ values for multiple ships are then compared to values for $SL^{W-H}(f)$ computed with the empirical Wales–Heitmeyer SL model (Wales and Heitmeyer, 2002).

The remainder of this paper is organized as follows. Section II discusses the acoustical measurements. Section III discusses prior assumptions about the ship motion and geophysical/geoacoustic characterization of the seabed and empirical constraints on the seabed model. Section IV defines the error function, inferred SLs, and PDFs. Sections V and VI provide the results and a conclusion, respectively.

II. ACOUSTIC MEASUREMENTS AND INITIAL PROCESSING

Merchant ship noise data were recorded on two VLAs deployed on the New England continental shelf during a time when the sound speed of the water column was approximately constant with depth. The locations of the two VLAs, the shipping lane, and the track of the *Viking Bravery* that deviated from the southern shipping lane are shown in Fig. 1(a). The start and end times of the processing intervals of merchant ships considered for analysis, shown in Table I, place the CPA time at about the midpoint time of the processed data.

For the ℓ th ship recording on the VLA, the measured pressure time series at the j th receiver, $p_{\ell j}(t)$, were processed with short-time fast Fourier transform (FFT) with a Hann window yielding the complex spectra $P_{\ell j}(t_i, f_k)$, with $i = 1, 2, \dots, N_t, k = 1, 2, \dots, N_f$, where N_t and N_f are the

number of time and frequency segments, respectively. The received level spectrogram (data) for the ℓ th ship recorded on the j th receiver is defined as

$$D_{\ell j}(t_i, f_k) = 10 \log_{10}(|P_{\ell j}(t_i, f_k)/1\mu\text{Pa}^2|), \quad (1)$$

with units of decibels re $(1\mu\text{Pa})^2/\text{Hz}$.

For this analysis, the spectrograms are processed in time intervals of about 20 min over the 200–750 Hz band, with a frequency spacing of 0.3815 Hz. An example of a processed spectrogram obtained from channel 05 on VLA 02 is shown in Fig. 1(b) for the merchant ship *Kalamata*. The peak and null structure at CPA time is a result of the coherent combination of direct, bottom, and surface reflected components.

An additional data sample from the ship *Viking Bravery* was collected at VLA 01 about 20 min after the recording was made on VLA 02. This data sample was held in reserve to test how well the implicit SL obtained from the data processing on VLA 02 generalized to data recorded on VLA 01. Only in the case of the *Viking Bravery* is a ship track reasonably aligned with the main sediment thickness map. The other tracks are skewed, and, thus, one would expect a greater lack of symmetry in the spectrograms for a single ship recorded at the two VLAs.

III. PRIOR MODELS

A. Ship motion and source

An idealized model for the motion of the merchant ships relative to an acoustic array is shown in Fig. 2. The range from the ship to the VLA for the i th time segment is

TABLE I. Merchant ships selected for analyses and time of recordings.^a

Index ℓ	Ship	JD	h	Start min:end min
1	<i>Kalamata</i>	83	18	10:33
2	<i>Tombarra</i>	90	10	30:56
3	<i>Viking Bravery</i>	90	07	10:33
4	<i>Maersk Matsuyama</i>	90	09	40:60
5	<i>Hafnia Green</i>	89	18	32:52

^aThe selected data samples were recorded on VLA 02.

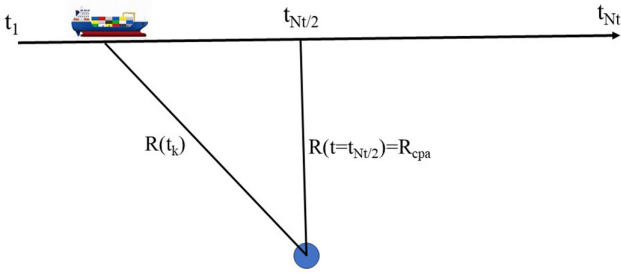


FIG. 2. (Color online) Idealized motion of merchant ships.

$$R_i = \sqrt{(R_{cpa})^2 + r^2(t_i)}, \quad (2)$$

where

$$r(t_i) = \begin{cases} (t_i - N_t/2)v, & t < t_{cpa}, \\ (t_i + N_t/2)v, & t > t_{cpa}, \end{cases} \quad (3)$$

and v is the speed of the ship. The analysis assumes that the ship motion is uniform, that the radiation is emitted at an effective point source at a constant depth, and that the environment is horizontally stratified. In reality these assumptions are seldom satisfied and can cause a time-frequency spectrogram to be asymmetric about the time axis at CPA time. An example of this asymmetry is evident in Fig. 1(b).

B. Prior sediment model and empirical constraints

In this work, two upper sediment layers are parameterized by a hybrid VGS model, as shown in Fig. 3. Below these layers is a fixed deep-sediment layering that was inferred in Knobles *et al.* (Knobles *et al.*, 2021; Knobles *et al.*, 2022) to model the very low frequency characteristics of the waveguide invariant. The hybrid VGS model uses the VGS parameterization to establish the sound speed, the density, and the attenuation at the surface of each sediment layer and a non-linear depth dependence (NLDD) parameterization of the sediment sound speed as a function of depth in each layer. The NLDD parameterization was formulated to characterize the empirical nature of observed low-angle bottom loss for different classes of seabed environments (Spofford, 1980).

The parameterization of the VGS model for each sediment layer includes layer thickness T , porosity N , grain size

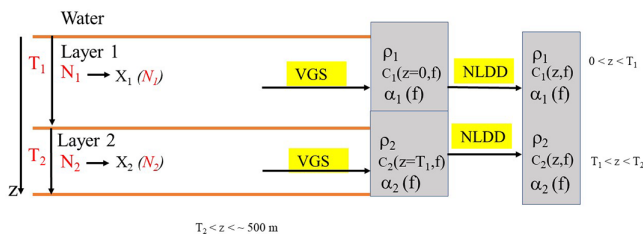


FIG. 3. (Color online) Two sediment layer model over fixed deep layers. The two sediment layers are parameterized by the hybrid VGS-NLDD model, and the fixed deep layer structure is taken from Knobles *et al.* (Knobles *et al.*, 2021; Knobles *et al.*, 2022).

μ_g , grain density ρ_g , grain bulk modulus K_g , bulk modulus K_0 , bulk density ρ_0 , strain hardening index n , and the viscous time constant τ . Not all of these parameters are independent. For example, the parameters μ_g , ρ_0 , and K_0 are dependent on N : i.e., $\mu_g(N)$, $\rho_0(N)$, and $K_0(N)$. Following the discussion by Buckingham (2005), an expression for grain size is

$$\mu_g(N) = \frac{2\Delta(2B - 1)}{1 - B}, \quad (4)$$

where

$$B = \left(\frac{1 - N}{1 - N_{\min}} \right)^{1/3} \quad (5)$$

with $N_{\min} = 0.37$. The roughness parameter is defined as $\Delta = 1 \mu\text{m}$. In units of the Krumbein ϕ scale (Krumbein, 1934), the grain size can be expressed as

$$\phi = -\log_2(\mu_g/\mu_0), \quad (6)$$

where $\mu_0 = 1000 \mu\text{m}$. Similarly, the bulk modulus and bulk density can be found by utilizing the low-frequency limit of the VGS model described by the Wood–Mallock equations (Wood, 1930; Mallock, 1910). With ρ_w as the density of the water,

$$\rho_0(N) = \rho_g + N(\rho_w - \rho_g). \quad (7)$$

Thus, if $\rho_g(N)$ is assumed known *a priori*, then $\rho_0(N)$ can be estimated. For a given value of N and K_g , the bulk modulus K_0 is estimated from

$$\frac{1}{K_0} = \frac{N}{K_w} + \frac{(1 - N)}{K_g}, \quad (8)$$

where K_w is an assumed water bulk modulus.

While K_g , ρ_g , n , and τ do not have analytical relationship to porosity, their empirical relationship to porosity can be estimated. The Wentworth scale (Wentworth, 1922) classifies sediments in terms of grain size or, equivalently, porosity. A Wentworth-inspired VGS sediment classification based on porosity is shown in Table II. The values for $K_g(N)$ and $\rho_g(N)$ in the different sediment classes are approximately established from the literature with the understanding that the values for K_g can have significant uncertainty. The values of $n(N)$ and $\log[\tau(N)]$ are deduced from collective attenuation measurements in the literature. For example, modeled values (not shown here) were compared to previously reported graphics of compressional sound speed ratio and attenuation of a medium sand (Zhou *et al.*, 2009; Zhou *et al.*, 2010; Richardson *et al.*, 2001; Carey and Evans, 1988) and a clayey sandy silt (Wilson *et al.*, 2020; Boyles, 1997). The modeled values were obtained from the VGS model, with the $X(N)$ relationships shown in Table II for a medium sand and clayey sandy silt. In addition to these examples, reported sound speed and

TABLE II. VGS and NLDD parameterization on Wentworth classification scale (Wentworth, 1922) with porosity as independent parameter.

Sediment type	N	ρ_g	kg	n	$\text{Log}(\tau)$	g	β
Granules	0.372	2650	36.0	0.12	-3.9208	5.0	-0.99
Very coarse sand	0.374	2650	36.0	0.111	-3.9208	5.0	-0.99
Coarse sand	0.378	2650	32.0	0.100	-3.9208	5.0	-0.99
Medium sand	0.385	2650	28.0	0.095	-3.9208	5.0	-0.985
Fine sand	0.399	2600	28.0	0.085	-3.9208	5.0	-0.975
Very fine sand	0.425	2600	28.0	0.080	-3.9208	5.0	-0.965
Coarse silt	0.471	2550	22.0	0.0785	-3.9208	5.0	-0.956
Silty sand	0.500	2600	19.0	0.0775	-2.9208	5.0	-0.956
Medium silt	0.543	2525	14.67	0.067	-1.9208	5.0	-0.945
Clayey sand silt	0.600	2500	13.67	0.065	3.0457	6.0	-0.938
Fine silt	0.640	2500	13.61	0.060	3.0457	4.0	-0.870
Silty clay	0.694	2500	13.55	0.0575	3.0457	3.5	-0.830
Very fine silt	0.735	2500	13.50	0.055	3.0457	3.0	-0.800
Clay	0.750	2500	13.50	0.045	3.0457	2.2	-0.800
Very soft clay	0.90	2500	8.850	0.045	3.0457	2.0	-0.800

attenuation data for clay from measurements in the Gulf of Mexico (Rubano, 1980; Lynch *et al.*, 1991; Collins *et al.*, 1992; Knobles *et al.*, 2003), a coarse silt sediment in the New England Bight (Potty *et al.*, 2003), a thick fine silt sediment in the Gulf of Oman (Sagers and Knobles, 2014), and a mixed sediment region of the Yellow Sea (Rogers *et al.*, 2000) were used to establish $n(N)$ and $\log_{10}(\tau)$ for different sediment classifications in Table II.

In Table II, $\log_{10}(\tau)$ is characterized by the two asymptotic values for a very soft clay and sand granules of 3.05 and -3.92, respectively, with a sudden change in values that occurs between silty sand and clayey sand-silt. This change is a reflection of not having enough sound speed and attenuation dispersion data for sediment classes containing various mixtures of sands and silts to estimate empirically the width on a classification scale of the transition from the VGS to the grain shearing (GS) limit. Future work is needed to better understand the nature of viscous effects in mixed sediments. While most of the results presented use K_g , n , and τ values that are related to N , as specified in Table II, in Sec. VB, τ , K_g , and n in the top sediment layer are varied randomly, independent of N , as a form of error analysis.

The concept of Table II is not new or unique. Hamilton and Bachman (Hamilton and Bachman, 1982; Bachman, 1985; Hamilton, 1979, 1980), Richardson and Briggs (1993), and Vidmar (1983) have all used a similar approach in sediment classification. The most important aspect in the current analysis that is different from the previous attempts at sediment classification is the use of a causal model for the seabed that restricts the frequency dispersion of the sound speed and attenuation to a Kramers-Kronig relationship (Toll, 1956; Jackson, 1975). The causality constraint acts as an important means to reduce the dimensionality of the problem and constrain the multi-dimensional volume of the parameter space in a physical manner.

In this study, N is allowed to vary randomly between an upper and lower bound. The values for the dependent variable are $X(N')$ where N' is the nearest porosity to the values

given in Table II. For a given value of N , values for $X(N)$ in Table II and the VGS model provide the surface ($z=0$) values for $\rho_0(z=0)$, the compressional attenuation $\alpha(f, z=0)$, and the surface compressional sound speed $C_0(f) = C(f, z=0)$. For this work, the gradients for the attenuation and density are assumed to be zero, and thus, $\rho_0(z) = \rho_0(z=0)$ and $\alpha(f, z) = \alpha(f, z=0)$. The depth-dependent sound speed in the mud sediment, $C(f, z)$, is assumed to be represented by a non-linear sound speed profile,

$$C(f, z) = \sqrt{C_0^2(f)(1 + \beta)^2 + 2C_0(f)(1 + \beta)gz - \beta C_0(f)},$$

$$0 \leq z \leq T_1, \tag{9}$$

with curvature parameter β and surface sound speed gradient g . The origins of this profile are closely related to early bottom loss studies in deep sediments (Spofford, 1980). In the limit that $\beta \rightarrow 0$, this profile is similar to that used in Chapman *et al.* (1984) for thick deep water sediments, with the exception that Eq. (9) does not contain a singularity at $z = C_0/2g$. This profile is consistent with the study made by Ogushwitz (1985), which indicated a near surface gradient for sandy sediments of about $g = 5 \text{ s}^{-1}$, and also approaches the value of 1 s^{-1} at a depth of 20 m given by Hamilton (1979) using $\beta = -0.99$. Also, $\lim_{\beta \rightarrow -1} C(z, f) = C_0(f)$.

Advantages of using the VGS model with sediment classes based on porosity include (1) a reduced-order model, (2) physically realistic sediments, and (3) an ability to make comparison with measured geophysical ground truth. The VGS model that includes viscoelastic effects of a linear response is based on a simple mechanical system with a Zener model (Carcione, 2014). Since the VGS model is a causal model, the attenuation is not a free parameter; this fact allows for the general ambiguity of SLs and attenuation to be mitigated with data samples corresponding to longer ranges. While there are other physical models, such as poro-elastic models, that can also provide adequate fits to the dispersion characteristics of, for example, the sediment sound speed, such models also have a greater number of independent parameters. For example, permeability, creep, and tortuosity are important parameters for poro-elastic models (Chotiros, 2017, 2021), but how to relate such parameters in a scheme that orders classification based on porosity, such as in the current approach, remains unknown.

IV. OPTIMIZATION APPROACH

A. Prior model

The inversion processing methodology, shown in Fig. 4, is initiated with a Monte Carlo sampling of the parameter space defined in Tables II and III. For each sampling of the parameter space θ , the hybrid VGS model and NLDD model are used to compute the inputs for a normal mode propagation model (Westwood *et al.*, 1996), which are used to calculate frequency-dependent modeled propagation loss, $\text{PL}_M(f, \theta, z_j)$ ($j = 1, 2, \dots, N_r$). Then, using the data D_ℓ , a time-averaged SL, $\text{SL}_\ell(\theta, f, z_j)$ is computed, which then

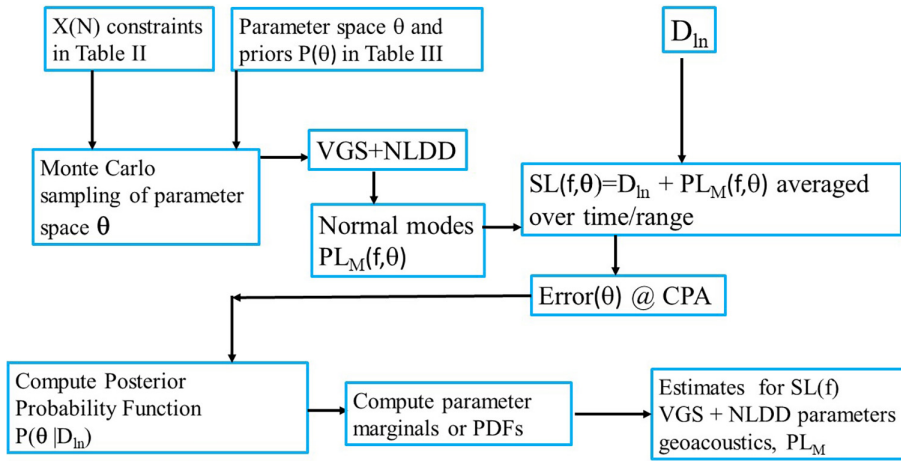


FIG. 4. (Color online) Processing analysis chain for merchant ship noise.

permits a value of the modeled received level to be computed at the CPA time for each sampling of θ .

The statistical optimization approach begins with defining the prior distribution. For this work, the priors include (1) identifying porosity as the independent variable and assuming that the other geophysical parameters with the VGS model are dependent parameters $X(N)$, (2) using two sediment layers, and (3) establishing the upper and lower parameter bounds in Table III. The *parameter vector* θ contains $[N_1, N_2, T_1, T_2, z_s, R_{cpa}]$, where N_1 and T_1 are the porosity and thickness of the first sediment layer, N_2 and T_2 are the porosity and thickness of the second sediment layer, z_s is an effective depth for the source, and R_{cpa} is the CPA range. The *volume* of θ is defined by the bounds shown in Table II: the prior distributions are assumed to be uniform between these upper and lower bounds.

B. Implicit SL and model transmission loss

In the implicit formulation (Koch, 2010; Tollefsen et al., 2022; Dosso and Wilmut, 2006; Knobles, 2015), SL is a function of the parameter space θ and the time-averaged SL for each receiver depth z_j is

$$SL_{\ell}(\theta, f_k, z_j) = \frac{1}{N_t} \sum_{i=1}^{N_t} (D_{\ell}(t_i, f_k, z_j) + PL_M(\theta, f_k, z_j, t_i)). \quad (10)$$

$D_{\ell}(t_i, f_k, z_j)$ represents the merchant ship spectrograms for the ℓ th data sample and the j th receiver on a VLA. The modeled

TABLE III. 6-D parameter space with upper and lower bounds.

Parameter	Unit	Bound	
		Lower	Upper
N_1	—	0.355	0.85
T_1	m	2	15
N_2	—	0.355	0.85
T_2	m	10	55
z_s	m	3	15
R_{cpa}	m	2500	4500

propagation loss, PL_M , is computed using a normal mode expansion of the acoustic field (Westwood et al., 1996). Using SL and PL_M , the modeled received level is

$$ML_{\ell}(\theta, t_{cpa}, f_k, z_j) = SL_{\ell}(\theta, f_k, z_j) - PL_M(\theta, f_k, z_j, t_{cpa}). \quad (11)$$

Also, the inferred measured propagation loss (PL_{mea}) is

$$(PL_{mea})_{\ell}(\theta, t_{cpa}, f_k, z_j) = SL_{\ell}(\theta, f_k, z_j) - D_{\ell}(t_{cpa}, f_k, z_j). \quad (12)$$

C. Posterior probability distribution

For the statistical analysis, the error function is evaluated at the CPA time, t_{cpa} , as

$$E_{\ell}(\theta, D_{\ell}) = \frac{1}{N_f N_r} \sum_{j=1}^{N_f} \sum_{k=1}^{N_r} (D_{\ell}(t_{cpa}, f_k, z_j) - ML_{\ell}(\theta, t_{cpa}, f_k, z_j))^2, \quad (13)$$

and is averaged over hydrophone number of the VLA and frequency. N_r is the total number of hydrophones.

Monte Carlo sampling of θ is performed and $E(\theta, D_{\ell})$ calculated for each data sample D_{ℓ} . After sampling, a useful quantity is the optimal solution or estimate,

$$\hat{\theta}_{\ell} \in \theta_{\ell} \text{ such that } E_{\ell}(\hat{\theta}_{\ell}, D_{\ell}) \leq E_{\ell}(\theta_{\ell}, D_{\ell}) \text{ for all } \theta_{\ell}. \quad (14)$$

The index ℓ attached to $\hat{\theta}_{\ell}$ signifies that $\hat{\theta}_{\ell}$ is linked directly to D_{ℓ} . However, $\hat{\theta}_{\ell}$ has no estimate of the uncertainty and represents a frequentist solution (Goodfellow et al., 2016).

After sampling $E(\theta, D_{\ell})$, the next step requires computing a conditional posterior probability density (PPD) for each data sample ℓ . For this purpose, the relative maximum entropy method (Kullback and Leibler, 1951) is employed. The conditional PPD using the relative maximum entropy method is

$$P(\theta|D_{\ell}) = P(\theta) \frac{\exp[-b_{\ell} E_{\ell}(\theta, D_{\ell}, t_{cpa}), D_{\ell}]}{Z_{\ell}}, \quad (15)$$

where Z_{ℓ} is the partition function,

$$Z_\ell = \int d\theta P(\theta) \exp[-b_\ell E_\ell(\theta, D_\ell, t_{cpa})], \quad (16)$$

and $P(\theta)$ is the prior distribution. The factor b_ℓ is analogous to $1/kT$ in statistical physics and is determined by solving the constraint integral equation

$$\langle E_\ell \rangle = \int d\theta P(\theta|D_\ell) E_\ell(\theta, D_\ell), \quad (17)$$

where the integration is over θ for fixed D_ℓ . Unlike a Bayesian dogma, which claims *a priori* knowledge of the statistics of the error function, the essence of maximum entropy is the assumption that the only information known prior to the measurements is a limited number of statistical moments. For example, if $\langle E_\ell \rangle$ is known, then computing b_ℓ becomes a straightforward matter of multidimensional integration via Eq. (17). Unfortunately Jaynes (1957a,b) never mentioned how to actually compute or estimate $\langle E_\ell \rangle$. One approach is to use multiple data samples to define uncertainty.

From the work in Bilbro and Van den Bout (1992), Tishby *et al.* (1989), and Levin *et al.* (1990), the *data-space* representation is used, as opposed to the *model-space* representation, to compute $\langle E_\ell \rangle$. This approach is useful because the integral is over $D = \{D_\ell\}$ with θ fixed,

$$\langle E_\ell \rangle \approx \int dD' P(D'|\hat{\theta}(D_\ell)) E_\ell(\hat{\theta}(D_\ell), D'), \quad (18)$$

where $P(D|\theta)$ is the likelihood function. For a finite number of data samples D_ℓ and assuming that all the ships transverse the same track at the same CPA range and effective source depth, $\langle E_\ell \rangle$ is approximated (Knobles *et al.*, 2012) as

$$\langle E_\ell \rangle \approx \frac{1}{N} \sum_{k=1}^N E(\hat{\theta}(D_\ell), D_k). \quad (19)$$

As discussed in Knobles (2015) the interpretation of the off diagonal terms in Eq. (19) requires clarification because in the current study the data samples are from different ships traversing different tracks and emitting broadband radiation from different effective depths. In the current analysis, the off diagonal terms must exclude the interchange of the k and ℓ indices that refer to source depth and CPA range. We can rewrite Eq. (19) to include this exclusion by introducing the following notation,

$$\hat{\theta} = (\hat{\theta}_{\text{geo}}, \hat{\theta}_{\text{source}}), \quad (20)$$

where $\theta_{\text{geo}} = [N_1, T_1, N_2, T_2]$ and $\theta_{\text{source}} = [z_s, R_{\text{cpa}}]$. The idea is that θ_{source} belongs to a specific ship, whereas θ_{geo} is associated with the seabed, which then permits $\langle E_\ell \rangle$ to be expressed as

$$\langle E_\ell \rangle \approx \frac{1}{N} \sum_{k=1}^N E(\hat{\theta}_{\text{geo}}(D_\ell), \hat{\theta}_{\text{source}}(D_k), D_k). \quad (21)$$

TABLE IV. $E_{\ell k}$, $\langle E_\ell \rangle$, and b_ℓ .^a

Ship	KAL ($k = 1$)	TOM ($k = 2$)	VB ($k = 3$)	MAT ($k = 4$)	HG ($k = 5$)	$\langle E_\ell \rangle$	b_ℓ
KAL ($\ell = 1$)	16.65	18.2	16.60	18.37	18.2	17.60	1.21
TOM ($\ell = 2$)	22.92	18.48	23.94	19.34	18.49	20.83	0.99
VB ($\ell = 3$)	20.64	22.29	21.0	23.03	22.29	21.85	2.11
MAT ($\ell = 4$)	25.24	21.65	25.21	20.57	21.65	22.86	0.84
HG ($\ell = 5$)	25.59	24.89	26.32	25.41	24.89	25.42	2.92

^aShip abbreviations: KAL, *Kalamata*; TOM, *Tombarra*; VB, *Viking Bravery*; MAT, *Maersk Matsuyama*; HG, *Hafnia Green*.

Conceptually, the off diagonal terms of E are deeply rooted in statistical mechanics. This paradigm can be used if one considers an acoustic measurement in the ocean is drawn from an *ensemble* of possible *states of a system* that are in *thermodynamic equilibrium with a heat bath*. Finally, the estimated value of $\langle E_\ell \rangle$ from Eq. (21) is then inserted into Eq. (17) for the purpose of computing b_ℓ , which then uniquely specifies the PPD in Eq. (15). A PDF (also called marginal probability distribution) for a parameter in the N -dimensional space is then obtained by integrating the PPD over the other $N-1$ nuisance parameters.

V. RESULTS

A. Multiship analysis

The results of the maximum entropy inversions are now presented for the five ships listed in Table I. Table IV shows the elements of the 5×5 matrix $E(\hat{\theta}_{\text{geo}}(D_\ell), \hat{\theta}_{\text{source}}(D_k))$, $\langle E_\ell \rangle$, and b_ℓ for all five ships. Then, using the PPD in Eq. (15), the PDFs for the six parameters in θ are obtained for each data sample. The estimated PDFs are shown in Fig. 5 for $\ell = 1, 2, 3, 4, 5$.

The expected parameter values $\mathcal{E}[X]$ and standard deviations $\sigma[X]$ for the values of a parameter X are computed using the PDFs (P_X) (derived from the PPD),

$$\mathcal{E}[X] = \int dx X P_X(x), \quad (22)$$

$$\sigma[X] = \int dx \sqrt{(\mathcal{E} - x)^2} P_X(x). \quad (23)$$

The resulting $\mathcal{E}[X]$ and $\sigma[X]$ of the parameters are presented in Tables V–IX. Also shown are θ_{peak} , defined such that $P(\theta_{\text{peak}}) \geq P(\theta)$ for all θ , and the optimal parameter values, $\hat{\theta}$.

Both Fig. 5 and the values in Tables V–IX provide insights into the parameters estimated by the maximum entropy method. Generally, the parameter values for N_1 and CPA range are well resolved. Parameter values for N_2 are not as well resolved as are those for N_1 . The resolution for T_2 is generally poor. With the exception of the *Matsuyama* data sample, which has the largest CPA range, the $P(\theta_{\text{peak}})$ values for the porosity N_1 are near the ground truth value of 0.6012 from an analysis of piston cores taken by United States Geological Survey (USGS) (Chaytor *et al.*, 2021). The marginal distributions for R_{cpa} show that R_{cpa} and the

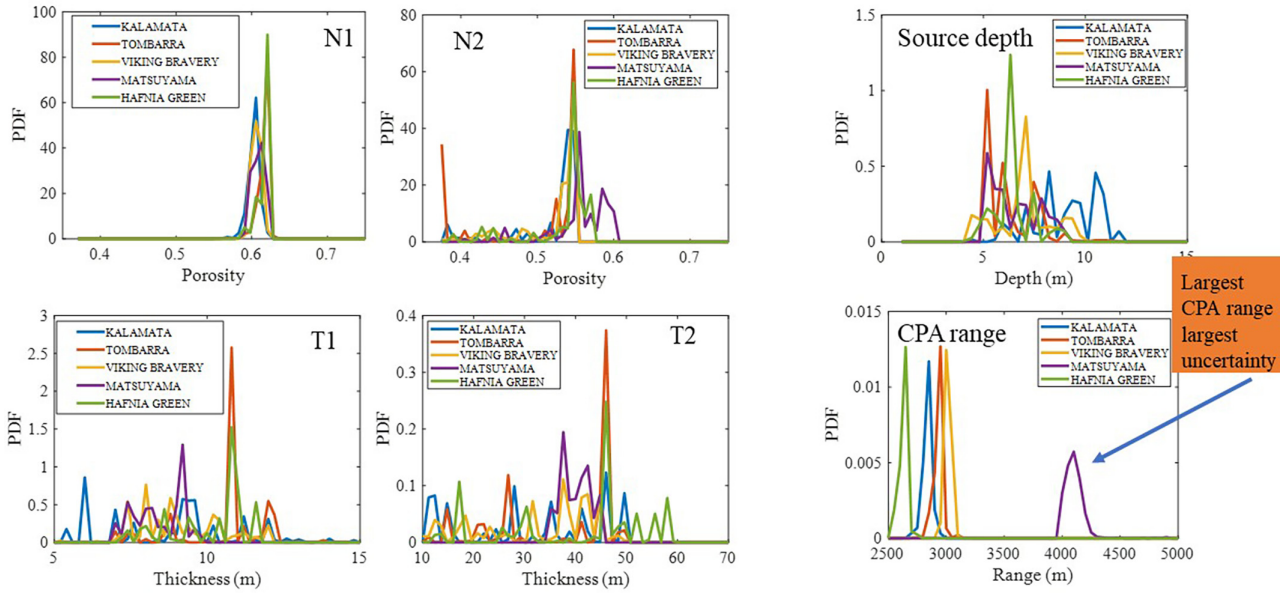


FIG. 5. (Color online) Marginal probability distribution functions for data samples $\ell = 1, 2, 3, 4, 5$.

TABLE V. Parameter statistics inferred from noise of *Kalamata*.

Parameter/statistic	N_1	T_1 (m)	N_2	T_2 (m)	z_s (m)	R_{cpa} (m)
$\hat{\theta}$	0.606	9.43	0.550	45.47	8.12	2841.2
θ_{peak}	0.606	6.0	0.548	46.0	8.22	2845.0
\mathcal{E}	0.603	8.85	0.522	31.60	9.07	2844.30
σ	0.007	2.05	0.045	13.94	1.51	37.71

TABLE VI. Parameter statistics inferred from noise of *Tombarra*.

Parameter/statistic	N_1	T_1 (m)	N_2	T_2 (m)	z_s (m)	R_{cpa} (m)
$\hat{\theta}$	0.617	10.77	0.549	45.47	5.28	2950.8
θ_{peak}	0.621	10.8	0.548	46.0	5.18	2960.0
\mathcal{E}	0.616	10.57	0.489	36.50	6.47	2940.5
σ	0.011	1.505	0.073	11.82	1.34	49.70

TABLE VII. Parameter statistics inferred from noise of *Viking Bravery*.

Parameter/statistic	N_1	T_1 (m)	N_2	T_2 (m)	z_s (m)	R_{cpa} (m)
$\hat{\theta}$	0.601	7.97	0.549	37.25	7.14	3015.60
θ_{peak}	0.598	8.0	0.548	37.16	7.08	3006.0
\mathcal{E}	0.605	8.41	0.541	36.51	6.82	3012.60
σ	0.006	0.98	0.018	6.28	0.84	15.38

TABLE VIII. Parameter statistics inferred from noise of *Matsuyama*.

Parameter/statistic	N_1	T_1 (m)	N_2	T_2 (m)	z_s (m)	R_{cpa} (m)
$\hat{\theta}$	0.616	9.20	0.553	37.53	5.18	4151.2
θ_{peak}	0.613	8.2	0.555	37.60	5.18	4100.0
\mathcal{E}	0.609	8.39	0.556	40.04	6.65	4111.3
σ	0.008	0.80	0.040	2.80	1.20	119.4

uncertainty σ are inversely related: The ships *Hafnia Green* and *Matsuyama* have the smallest and largest CPA ranges and range uncertainty, respectively. We may ascribe this to an increase in the uncertainty of the localization with increasing range. Finally, the average optimal values of z_s and σ for all the ships are 6.14 m and a 1.2 m, respectively. The small value of σ suggests that the Lloyd's mirror effect was being adequately modeled.

To further test the inferred parameter values, comparisons are shown in Figs. 6 and 7 and Figs. 8 and 9 of PL_{mea} and PL_M at the CPA times for all 16 hydrophone elements for the *Kalamata* and *Tombarra* data samples, respectively. These two data samples are separated in time by about 1 week. However, the CPA range and source speeds for the two ships are quite similar. The PL_M and PL_{mea} comparisons for the *Kalamata* and the *Tombarra* data samples are evaluated at the optimal values $\hat{\theta}_{\ell=1}$ and $\hat{\theta}_{\ell=2}$, respectively. The model and data PL comparisons for $\ell = 3, 4, 5$ (not shown here) are similar.

The PL_M captures the *envelope* of the peak and null structure of PL_{mea} but is unable to capture the observed highly irregular *hash* that is observed to be superimposed on the envelope. The optimal values of the E_ℓ occurs for values of N_2 of about 0.55 for both data samples. This value of N_2 is high enough to reduce the cause of the perturbations of the envelope structure by reducing the magnitude of the reflection coefficient at the first and second layer interface.

TABLE IX. Parameter statistics inferred from noise of *Hafnia Green*.

Parameter/statistics	N_1	T_1 (m)	N_2	T_2 (m)	z_s (m)	R_{cpa} (m)
$\hat{\theta}$	0.617	10.77	0.549	45.47	6.13	2632.7
θ_{peak}	0.621	10.80	0.548	46.0	6.32	2650.0
\mathcal{E}	0.616	10.08	0.534	40.24	6.43	2631.0
σ	0.008	1.25	0.043	13.83	0.96	37.06

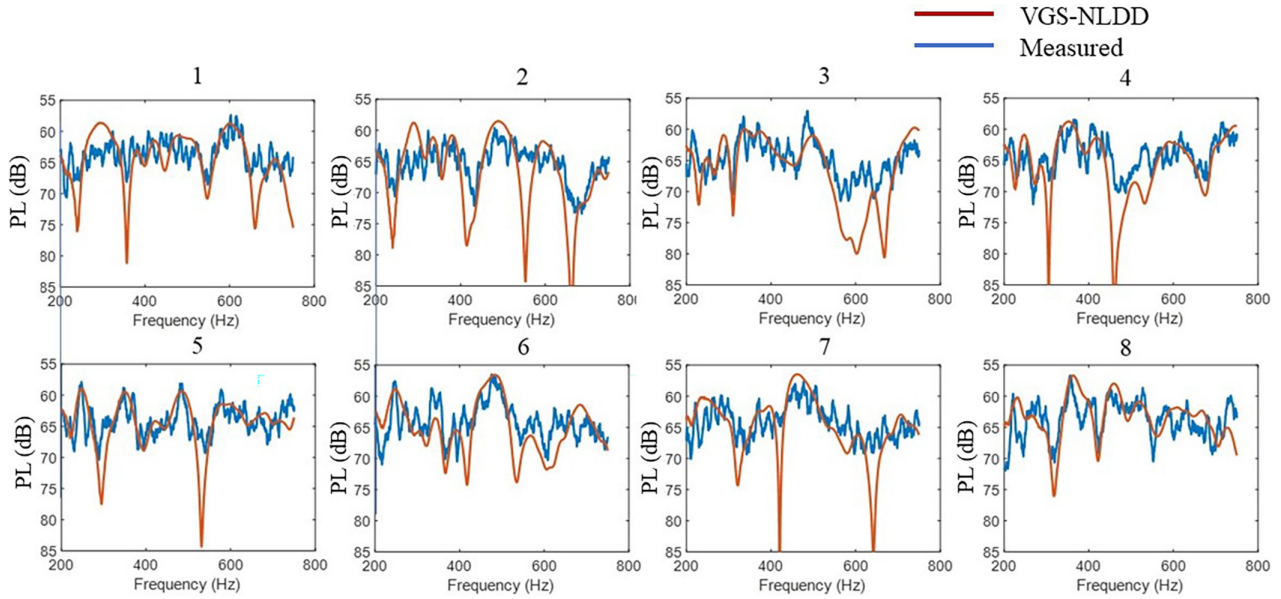


FIG. 6. (Color online) Model-measured PL comparison at CPA range for phones 1 to 8 of Scripps Marine Physical Laboratory (MPL) VLA 02 for recordings of the cargo ship *Kalamata*.

Lower values of N_2 result in an irregular *hash* structure similar to the observed PL_{mea} ; however, it is at the expense of an increase in the error function away from $E(\hat{\theta})$.

The measured-model comparison of time-frequency propagation loss (PL) for channel 08 of the *Kalamata* and the *Tombarra* are shown in Figs. 10 and 11, respectively, over time windows of about 20 min. The PL_{mea} is computed using Eq. (12). Qualitatively the agreement for both data samples is good. In summary, the PL_M captures the envelope structure of PL_{mea} , which corresponds to the lower grazing angles. Such a model may not be adequate at shorter ranges or equivalently at high grazing angles.

The results for $SL(\hat{\theta})$ for all receivers (channels 1 to 16) are shown in Fig. 12 for the data samples collected at VLA

02 [panels (a)–(e)] and VLA 01 [panel (f)]. A best-fit Wales–Heitmeyer curve (Wales and Heitmeyer, 2002),

$$SL^{W-H}(f) = S_0 - 10 \log_{10}(f^{3.594}) + 10 \log_{10}((1 + [f/340]^2)^{0.917}), \quad (24)$$

is included as the smooth black line where S_0 has been adjusted for an optimal fit. The peaks at approximately 300 Hz are not due to the merchant ship, but rather the RV *Endeavour*, which was operating in the area of VLAs 01 and 02. Except for CPA range, all parameters for the SL inference used for the VLA 02 analysis for the *Viking Bravery* data sample were utilized to infer the SLs for the *Viking Bravery* data sample collected on VLA 01 data. An optimal

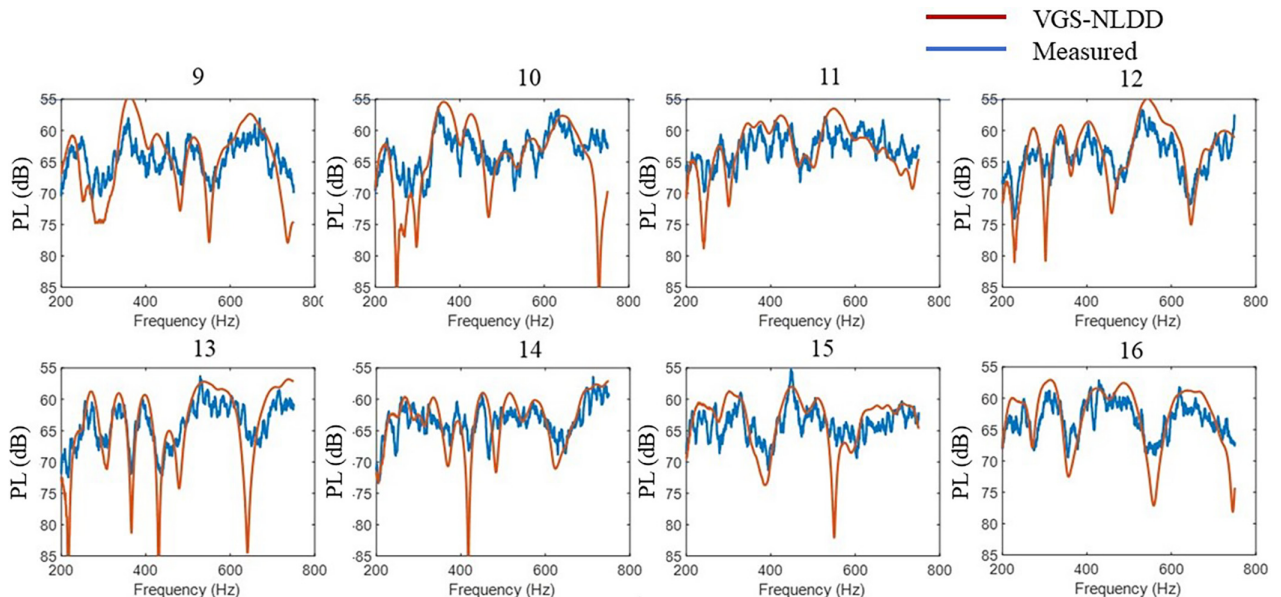


FIG. 7. (Color online) Model-measured PL comparison at CPA range for phones 9 to 16 of MPL VLA 02 for recordings of the cargo ship *Kalamata*.

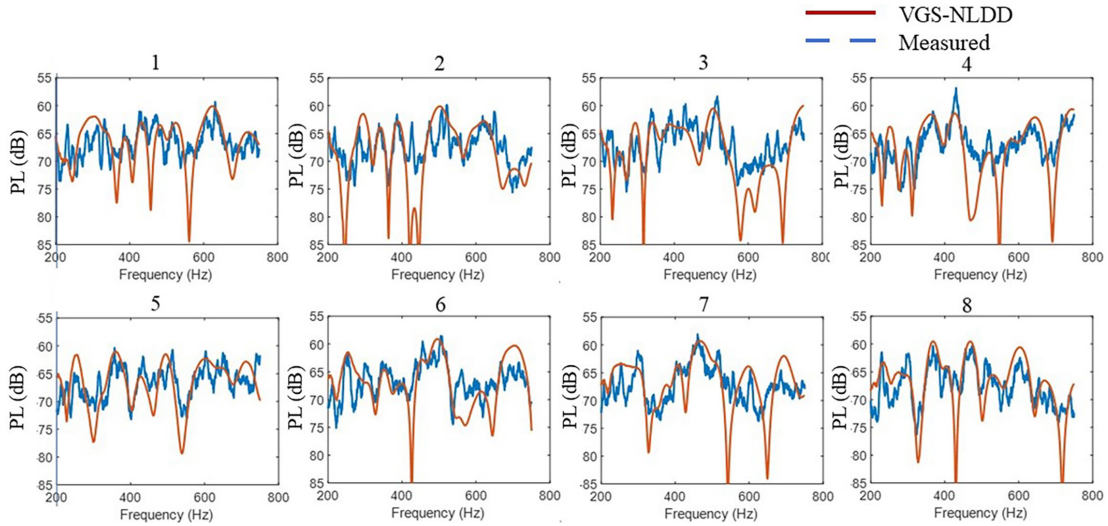


FIG. 8. (Color online) Model-measured PL comparison at CPA range for phones 1 to 8 of MPL VLA 02 for recordings of the cargo ship *Tombarra*.

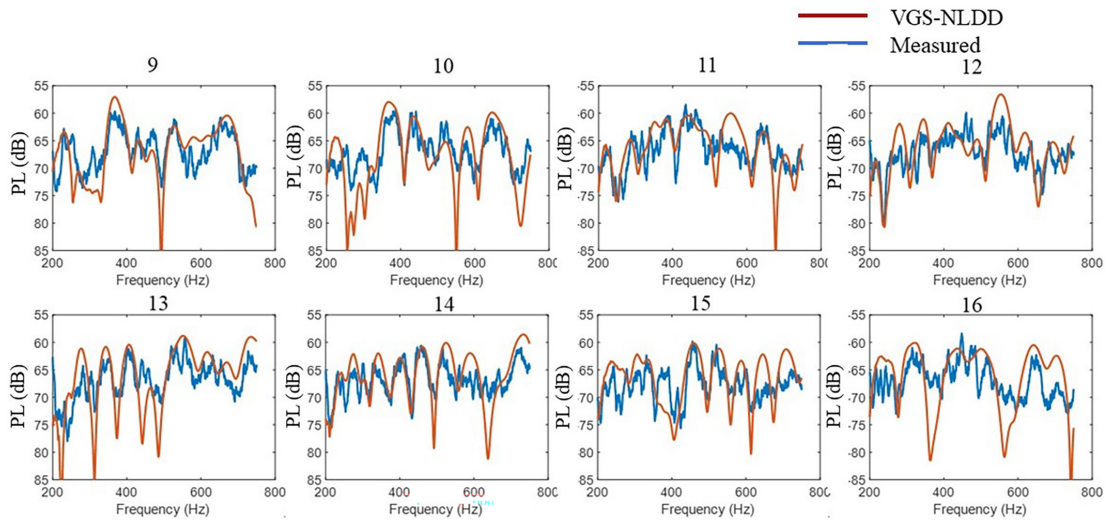


FIG. 9. (Color online) Model-measured PL comparison at CPA range for phones 9 to 16 of MPL VLA 02 for recordings of the cargo ship *Tombarra*.

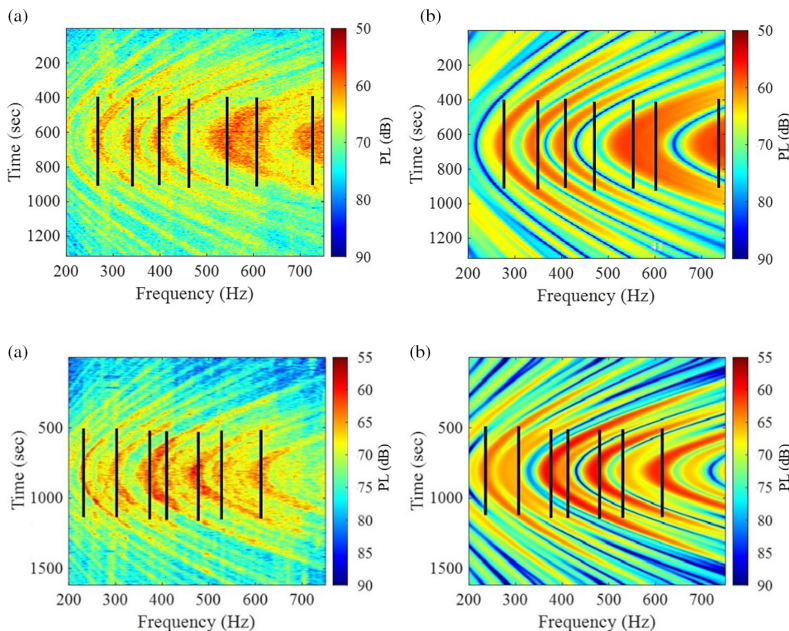


FIG. 10. (Color online) Model-measured comparison of PL from recordings on channel 13 of passage of the cargo ship *Kalamata*, (a) inferred measured PL, and (b) modeled PL with normal modes using $\hat{\theta}$. The inferred ship speed parameter value is 16.3 kn. The black lines indicate the observed frequencies with peaks at t_{cpa} .

FIG. 11. (Color online) Model-measured comparison of PL from recordings on channel 08 of passage of the cargo ship *Tombarra*, (a) inferred measured PL, and (b) modeled PL with normal modes using $\hat{\theta}$. The inferred ship speed parameter value is 16.08 kn. The black lines indicate the observed frequencies with peaks at t_{cpa} .

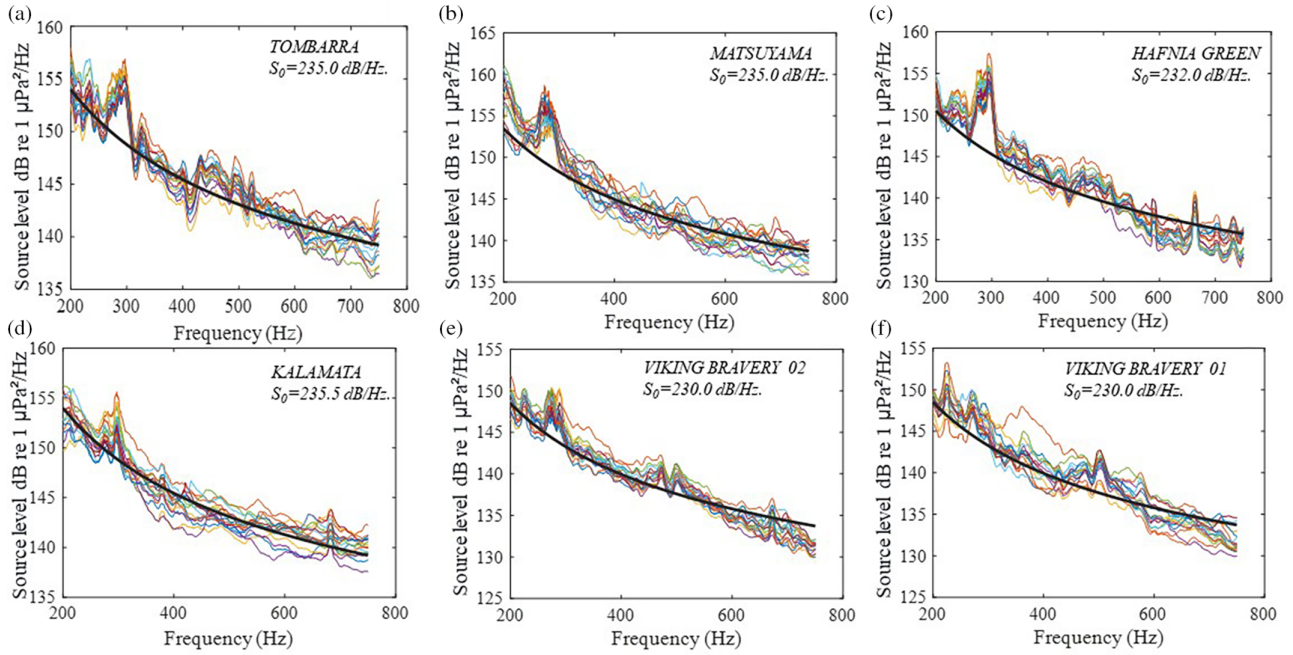


FIG. 12. (Color online) $SL(\hat{\theta})$ with a best fit of the Wales–Heitmeyer ensemble empirical relationship for data samples collected on VLA 02 during passage of merchant ships (a) *Tombarra*, (b) *Matsuyama*, (c) *Hafnia Green*, (d) *Kalamata*, and (e) *Viking Bravery* and (f) data sample collected on VLA 01 during passage of *Viking Bravery*. The different colored lines are the inferred SLs for the 16 channels of the VLA. The smooth black line shows the Wales–Heitmeyer ensemble formula for merchant ship levels for a best-fit value for S_0 .

CPA range value for the VLA 01 data sample was found to be 3350m. For Figs. 12(d) and 12(f), the same Wales–Heitmeyer curve with $S_0 = 230$ dB re $1 \mu\text{Pa}^2/\text{Hz}$ is shown for both plots. While the variance of the VLA 02 set of SL values for the 16 channels is slightly smaller than those for the VLA 01 data sample, $SL^{W-H}(f)$ provides a qualitative fit for the mean levels for both data samples. This comparison provides a measure of confidence in the proposed methodology of inferring merchant ship SLs in bottom-limited ocean environments.

B. Extension of parameter space to include K_g , n , and $\log_{10}(\tau)$ in top sediment layer

In Sec. III B, K_g , $\log_{10}(\tau)$, and n are considered fully dependent parameters of N and held fixed at discrete values of N (as listed in Table II) that essentially followed the

Wentworth scale. Another series of optimizations was performed in which K_g , $\log_{10}(\tau)$, and n in the top layer are varied independent of N with Monte Carlo sampling. The resulting nine-dimensional (9-D) θ values, which include upper and lower parameter bounds for K_g , $\log_{10}(\tau)$, and n , are shown in Table X. A statistical inversion was made for the 9-D θ space, and the resulting expected and standard deviation of θ_ℓ for the *Tombarra* data sample are shown in Table XI. A comparison of Table XI to Table VI, which is for the six-dimensional (6-D) space, provides the ratios of σ from the PDFs for the 9-D to the 6-D θ . For N_1 , T_1 , N_2 , T_2 , z_s , and R_{cpa} the ratios are $0.286/0.011 = 26$, $2.94/1.51 = 1.95$, $0.619/0.073 = 8.5$, $14.99/11.82 = 1.27$, $1.07/1.34 = 0.80$, and $69.31/49.70 = 1.39$, respectively. With the exception of z_s the standard deviation of parameter values for the 9-D parameter space is larger than those for the 6-D space with constraints. Finally, the SL for the *Tombarra* optimal solutions for the 6-D and 9-D parameter space θ are shown in Fig. 13. It is observed that, qualitatively, the variance of SL is about the same for Figs. 12(a) and 12(b).

TABLE X. 9-D parameter space with upper and lower bounds.

Parameter	Unit	Bound	
		Lower	Upper
N_1	—	0.355	0.85
T_1	m	2	15
N_2	—	0.355	0.85
T_2	m	10	55
z_s	m	3	15
R_{cpa}	m	2500	4500
n_1	—	0.05	0.15
$K_{g,1}$	GPa	13	40
$\text{Log}_{10}(\tau_1)$	—	-4	4

TABLE XI. Parameter statistics of 9-D parameter space inferred from noise of *Tombarra*.

Parameter/ statistic	N_1	T_1 (m)	N_2	T_2 (m)	Z_s (m)	R_{cpa} (m)	n_1	K_g (GPa)	Log (τ)
$\hat{\theta}$	0.619	10.99	0.548	21.35	5.064	2959.5	0.057	14.09	2.95
θ_{peak}	0.610	10.58	0.533	20.53	5.79	3105	0.054	13.0	2.325
\mathcal{E}	0.631	9.30	0.540	31.14	6.15	2989.0	0.056	14.036	1.94
σ	0.286	2.941	0.619	14.93	1.07	69.31	0.0079	1.40	1.41

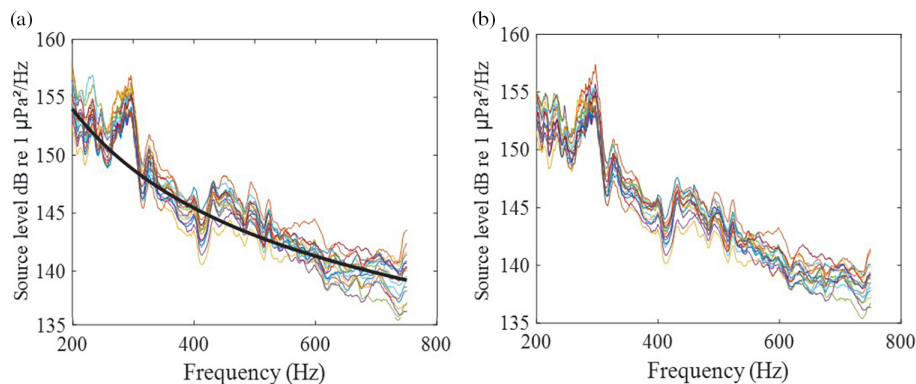


FIG. 13. (Color online) Comparison of the SLs for the *Tombarra* optimal solutions for (a) the 6-dimensional parameter space θ and (b) the 9-dimensional parameter space. The smooth black line is the same as in Fig. 12.

VI. CONCLUSION

A method was introduced where frequency-dependent SLs of merchant ships are inferred from acoustic measurements made in bottom-limited ocean environments. The method is based on the observation that the broadband acoustic features at CPA contain significant information content on both the source properties and the seabed characteristics. The inferred SLs are connected to the statistical inference of the PL, which is parameterized by the properties of an effective source depth, a CPA range, and a Wentworth classification scale based on a multi-layered VGS model with empirical constraints.

The method was tested using noise from merchant ships recorded on a vertical line array in the New England Mudpatch in 2017 that were analysed for the information content of both seabed geophysical and source parameters. The data collection was made on two VLAs in about 75 m of water with an approximate isospeed water column. A feature-based maximum entropy algorithm utilized acoustic data samples processed in the 200–750 Hz band from five merchant ships while they were located at the CPA to the VLAs. Features result from coherent effects from both sea surface and seabed. The physical constraints imposed by the hybrid VGS model allow for meaningful comparisons of measured and modeled PLs using estimated seabed parameters. The inferred implicit SLs for five merchant ships were then compared to the best fit of the Wales–Heitmeyer model. Above 200 Hz, the Wales–Heitmeyer model captures the inferred frequency dependence of the SLs.

A limited error analysis was performed on the use of the empirical parameter constraints enacted in Table I. Instead of using the empirical relationships for $K_g(N)$, $\tau(N)$, and $n(N)$ in Table I for the first sediment layer, the parameter space was extended from six dimensions to nine dimensions. For the specific type of sediment where the data samples were collected, a clayey sand silt (mud), the optimal values in the 9-D space suggest that the error of determining SL incurred by using the empirical relationships $X(N)$ appears small. Other sediment types may require additional study to establish suitable constraints for $K_g(N)$, $\tau(N)$, and $n(N)$.

ACKNOWLEDGMENT

This work received funding from Office of Naval Research Contract No. N00014-22-P-2007.

AUTHOR DECLARATIONS

Conflict of Interest

The authors have no conflicts to disclose.

DATA AVAILABILITY

The data that support the findings of this study are available from William Hodgkiss upon reasonable request.

- Bachman, R. T. (1985). “Acoustic and physical property relationships in marine sediments,” *J. Acoust. Soc. Am.* **78**, 616–621.
- Bilbro, G. L., and Van den Bout, D. E. (1992). “Maximum entropy and learning theory,” *Neural Comput.* **4**(6), 839–853.
- Boyles, F. A. (1997). “Observations on attenuation and shear-wave velocity in fine-grained, marine sediments,” *J. Acoust. Soc. Am.* **101**(1), 3385–3397.
- Buckingham, M. J. (2000). “Wave propagation, stress relaxation, and grain-to-grain shearing in saturated, unconsolidated marine sediments,” *J. Acoust. Soc. Am.* **108**(6), 2796–2815.
- Buckingham, M. J. (2005). “Compressional and shear wave properties of marine sediments: Comparisons between theory and data,” *J. Acoust. Soc. Am.* **117**(1), 137–152.
- Buckingham, M. J. (2007). “On pore-fluid viscosity and the wave properties of saturated granular materials including marine sediments,” *J. Acoust. Soc. Am.* **136**(5), 2478–2488.
- Carcione, J. M. (2014). *Wave Fields in Real Media: Wave Propagation in Anisotropic, Anelastic, Porous and Electromagnetic Media*, 3rd ed. (Elsevier, Amsterdam), Chap. 2.
- Carey, W. M., and Evans, R. E. (1988). “Frequency dependence of sediment attenuation in two low-frequency shallow-water acoustic experimental data sets,” *IEEE J. Ocean. Eng.* **23**(4), 439–447.
- Chapman, N. R., Barrodale, I., and Zala, C. A. (1984). “Measurement of sound-speed gradients in deep-ocean sediments using 11 deconvolution techniques,” *IEEE J. Ocean. Eng.* **9**(1), 26–30.
- Chaytor, J. D., Ballard, M. S., Buczkowski, B. J., Goff, J. A., Lee, K. M., Reed, A. H., and Boggess, A. A. (2021). “Measurements of geologic characteristics and geophysical properties of sediments from the New England Mud Patch,” *IEEE J. Ocean. Eng.* **47**, 503–530.
- Chotiros, N. P. (2017). *Acoustics of the Seabed as a Poroelastic Medium* (Springer, Cham, Switzerland), Chaps. 4 and 5.
- Chotiros, N. P. (2021). “A porous medium model for mud,” *J. Acoust. Soc. Am.* **149**(1), 629–644.
- Collins, M. D., Kuperman, W. A., and Schmidt, H. (1992). “Nonlinear inversion for ocean-bottom properties,” *J. Acoust. Soc. Am.* **92**(5), 2770–2783.

- Crocker, S. E., Nielsen, P. L., Miller, J. H., and Siderius, M. (2014). "Geoacoustic inversion of ship radiated noise in shallow water using data from a single hydrophone," *J. Acoust. Soc. Am.* **138**(5), EL362–EL368.
- Dozzo, S. E., and Wilmut, M. J. (2006). "Data uncertainty estimation in matched-field geoacoustic inversion," *IEEE J. Ocean. Eng.* **31**, 470–479.
- Gassmann, S. M., Wiggins, S. M., Wiggins, S. M., and Hildebrand, J. A. (2017). "Deep-water measurements of container ship radiated noise signatures and directionality," *J. Acoust. Soc. Am.* **142**(3), 1563–1574.
- Goodfellow, I., Bengio, Y., and Courville, A. (2016). *Deep Learning* (MIT Press, Cambridge, MA), Chap. 4.
- Gray, L. M., and Greeley, D. S. (1980). "Source level model for propeller blade rate radiation for the world's merchant fleet," *J. Acoust. Soc. Am.* **67**(1), 516–522.
- Hamilton, E. L. (1979). "Sound velocity gradients in marine sediments," *J. Acoust. Soc. Am.* **65**(4), 909–922.
- Hamilton, E. L. (1980). "Geoacoustic modeling of the sea floor," *J. Acoust. Soc. Am.* **68**(5), 1313–1340.
- Hamilton, E. L., and Bachman, R. T. (1982). "Sound velocity and related properties of marine sediments," *J. Acoust. Soc. Am.* **72**, 1891–1904.
- Jackson, J. D. (1975). *Classical Electrodynamics*, 2nd ed. (Wiley, New York), Chap. 7.10.
- Jaynes, E. (1957a). "Information theory and statistical mechanics," *Phys. Rev.* **106**(4), 620–630.
- Jaynes, E. (1957b). "Information theory and statistical mechanics II," *Phys. Rev.* **108**(2), 171–630.
- Jiang, P., Lin, J., Sun, J., Yi, X., and Shan, Y. (2020). "Source spectrum model for merchant ship radiated noise in the Yellow Sea of China," *Ocean. Eng.* **216**, 107607.
- Knobles, D. P. (2015). "Maximum entropy inference of seabed attenuation parameters using ship radiated broadband noise," *J. Acoust. Soc. Am.* **138**(3), 3563–3575.
- Knobles, D. P., Koch, R. A., Thompson, L. A., and Focke, K. C. (2003). "Broadband sound propagation in shallow water and geoacoustic inversions," *J. Acoust. Soc. Am.* **113**(1), 205–222.
- Knobles, D. P., Neilsen, T. B., Bonnel, J., Hodgkiss, W. A., Lin, Y. T., and Wilson, P. S. (2022). "Maximum entropy inference of seabed properties using waveguide invariant features from surface ships," *J. Acoust. Soc. Am.* **151**, 2885–2891.
- Knobles, D. P., Sagers, J., and Koch, R. A. (2012). "Maximum entropy approach for statistical inference in an ocean acoustic waveguide," *J. Acoust. Soc. Am.* **131**(2), 1087–1101.
- Knobles, D. P., Wilson, P. S., Hodgkiss, W. A., and Neilsen, T. B. (2021). "Influence of seabed on very low frequency sound recorded during passage of merchant ships on the New England shelf," *J. Acoust. Soc. Am.* **149**, 3294–3300.
- Koch, R. A. (2010). "Proof of principle for inversion of vector sensor array data," *J. Acoust. Soc. Am.* **128**(2), 590–599.
- Krumbein, W. C. (1934). "Size frequency distributions of sediments," *J. Sedimentary Res.* **4**, 65–77.
- Kullback, S., and Leibler, R. A. (1951). "On information and sufficiency," *Ann. Math. Statist.* **22**(1), 79–86.
- Levin, E., Tishby, N., and Solla, S. A. (1990). "A statistical approach to learning and generalization in layered neural networks," *Proc. IEEE* **78**(10), 1568–1574.
- Lynch, J. F., Rajan, S. D., and Frisk, G. V. (1991). "A comparison of broadband and narrow-band modal inversions for bottom geoacoustic properties at a site near Corpus Christi, Texas," *J. Acoust. Soc. Am.* **89**(1), 648–665.
- MacGillivray, A. O., Martin, S. B., Ainslie, M. A., Dolman, J. N., Li, Z., and Warner, G. A. (2023). "Measuring vessel underwater radiated noise in shallow water," *J. Acoust. Soc. Am.* **153**, 1506–1524.
- Mallock, A. (1910). "The damping of sound by frothy liquids," *Proc. R. Soc.* **84**(A572), 391–395.
- McKenna, M. F., Ross, D., Wiggins, S. M., and Hildebrand, J. A. (2012). "Underwater radiated noise from modern commercial ships," *J. Acoust. Soc. Am.* **131**, 92–103.
- Ogushwitz, P. R. (1985). "Applicability of the Biot theory. III. Wave speeds versus depth in marine sediments," *J. Acoust. Soc. Am.* **77**(2), 453–464.
- Potty, G. R., Miller, J. H., and Lynch, J. P. (2003). "Inversion for sediment geoacoustic properties at the New England Bight," *J. Acoust. Soc. Am.* **114**, 1874–1887.
- Richardson, M. D., and Briggs, K. B. (1993). "On the use of acoustic impedance values to determine sediment properties," in *Acoustic Classification and Mapping of the Seabed* (Bath University Press, Bath, England).
- Richardson, M. D., Briggs, K. B., Bibee, L. D., Jumars, P. A., Sawyer, W. B., Albert, D. B., Bennett, R. H., Berger, T. K., Buckingham, M. J., Chotiros, N. P., Dahl, P. H., Dewitt, N. T., Fleisher, P., Flood, R., Greenlaw, F. I., Charles, D. V., Holliday, M. H., Hulbert, M. P., Hutnak, P. D., Jackson, J. S., Jaffe, H. P., Johnson, D. L., Lavoie, A. P., Lyons, C. S., Martens, D., McGehee, E., Moore, K. D., Orsi, T. H., Piper, J. N., Ray, R. I., Reed, A. H., Self, R. F. L., Schmidt, J. L., Schock, S. G., Simonet, F., Stoll, R. D., Tang, D., Thistle, D. E., Thorsos, E. I., Walter, D. J., and Wheatcroft, R. A. (2001). "Overview of SAX99: Environmental considerations," *IEEE J. Ocean. Eng.* **26**(1), 26–53.
- Rogers, P. H., Zhou, J. X., Zhang, X. Z., and Li, F. (2000). "Seabottom acoustic parameters from inversion of Yellow Sea experimental data," in *Experimental Acoustic Inversion Methods for Exploration of the Shallow Water Environment*, edited by A. Caiti, J.-P. Hermand, S. M. Jesus, and M. B. Porter (Springer, Dordrecht, Netherlands).
- Rubano, L. A. (1980). "Acoustic propagation in shallow water over a low-velocity bottom," *J. Acoust. Soc. Am.* **67**(1), 1608–1613.
- Sagers, J. D., and Knobles, D. P. (2014). "Statistical inference of seabed sound-speed structure in the Gulf of Oman Basin," *J. Acoust. Soc. Am.* **135**(5), 3327–3337.
- Spofford, C. W. (1980). "Inference of geo-acoustic parameters from bottom-loss data," in *Bottom-Interacting Ocean Acoustics*, NATO Conference Series Book Series, Vol. 5, edited by W. A. Kuperman and F. B. Jensen (Plenum Press, New York), pp. 159–171.
- Tishby, N., Levin, E., and Solla, S. A. (1989). *Consistent Inference of Probabilities in Layered Networks: Predictions and Generalization* (IJCNN, IEEE, New York), Chap. II, pp. 403–410.
- Toll, J. S. (1956). "Causality and the dispersion relation: Logical foundations," *Phys. Rev.* **104**, 1760–1770.
- Tollefsen, D., Hodgkiss, S. E., Dozzo, S., Bonnel, J., and Knobles, D. P. (2022). "Probabilistic estimation of merchant ship source levels in an uncertain shallow-water environment," *IEEE J. Ocean. Eng.* **47**(3), 647–665.
- Vidmar, P. J. (1983). "Linked sets of acoustical processes and geoacoustic profiles describing the interaction of sound with a class of sea-floor structure," in *Acoustics and the Sea-Bed*, edited by N. G. Pace (Bath University Press, Bath, England), pp. 81–87.
- Wales, S. C., and Heitmeyer, R. M. (2002). "An ensemble source spectra model for merchant ship-radiated noise," *J. Acoust. Soc. Am.* **111**, 1211–1231.
- Wentworth, C. (1922). "A scale of grade and class terms for clastic sediments," *J. Geol.* **30**(5), 377–392.
- Westwood, E. K., Tindle, C. T., and Chapman, N. R. (1996). "A normal mode model for acousto-elastic ocean environments," *J. Acoust. Soc. Am.* **100**, 3631–3645.
- Wilson, P. S., Knobles, D. P., and Neilsen, T. A. (2020). "Guest Editorial: An overview of the seabed characterization experiment," *IEEE J. Ocean. Eng.* **45**(1), 1–13.
- Wood, A. B. (1930). *A Textbook of Sound* (MacMillan, New York), Chap. 2.
- Zhou, J. X., Zhang, X. Z., and Knobles, D. P. (2009). "Low frequency geoacoustic model for the effective properties of sandy sea bottoms," *J. Acoust. Soc. Am.* **125**, 2847–2866.
- Zhou, J. X., Zhang, X. Z., Rogers, P. H., and Jarzynski, J. (2010). "Geoacoustic parameters in a stratified sea bottom from shallow-water acoustic propagation," *J. Acoust. Soc. Am.* **128**(2), 578–589.